

3D/2D Projected Shape Sensitivity Analysis of Total Joint Arthroplasty Implants

Andrew James Jensen, Scott Banks, Ph.D.

Abstract

Recent methods in computer vision and machine learning have enabled fully-autonomous kinematics measurement for Total Knee Arthroplasty implant components. Unfortunately, this same performance does not translate to reverse Total Shoulder Arthroplasty implants. This study explores relating 3D implant orientation to 2D projection sensitivity using the Invariant Angular Radial Transform Descriptor (IARTD). Minor rotational differences yielded negligible shape changes along near-symmetric dimensions like humeral internal-external rotation and tibial internal/external axis. Furthermore, axes problematic for registration correlated with lower descriptor sensitivity. Overall, symmetrical geometries and orientations intrinsically limit extractable silhouette information. However, incorporating bony anatomical landmarks as optimization constraints shows promise for overcoming ambiguity and registration difficulties.

Introduction

Understanding the in-vivo kinematics of total joint replacement has been essential in implant design, post-operative assessment, and predicting wear and failure patterns for nearly three decades [8, 4, 5]. Recent advancements in computer vision and machine learning have enabled these analyses for total knee arthroplasty (TKA) in a fully autonomous and clinically practical setting, utilizing single-plane fluoroscopy [6, 9]. However, using only a single camera inherently limits the process due to loss of depth perception and the introduction

of ambiguous projected shapes during optimization [7, 15, 23, 3]. This limitation particularly affected mediolaterally symmetric tibial implants, leading to a phenomenon known as “symmetry traps.” In these cases, two distinct 3D orientations of the implant would yield indistinguishable 2D projected geometries. To address this, a machine learning algorithm was developed, trained to recognize true anatomic orientations and correct images caught in such optimization minima [10]. However, this approach still necessitated that the symmetric implant optimize into one of the two potential local minima corresponding to the identified “symmetry trap”.

Unfortunately, when the same optimization routine and cost function [7, 9] were applied to reverse total shoulder arthroplasty (rTSA), they significantly underperformed compared to total knee arthroplasty implants. This suboptimal optimization manifested in two primary ways. Firstly, there was a consistent error along the internal/external rotation axis. This axis not only represents near-rotational symmetry but is also the axis whose features are most often occluded by the glenosphere implant in frontal-plane fluoroscopy. Secondly, the optimization resulted in a distal shift of the implant. This shift meant that while the local minima correctly registered the humeral stem, they failed to do so for the humeral cup.

This pattern of failure prompted a deeper exploration into the psychology of shape [1, 2], underscoring the significance of high curvature as a salient feature in binary shapes. Additionally, binary distance metric studies [17, 18] emphasized the need to align the cost-function metric with the problem, considering the data’s underlying structure. In response to these new findings, and to address the challenges identified with rTSA kinematics optimization, we developed two novel cost functions.

To integrate high curvature regions into a novel cost function, we applied Menger’s discrete curvature algorithm [14] to the projected implant’s contour. This algorithm facilitated the algorithmic selection of high curvature regions. These regions were then utilized in a *Modified Asymmetric Surface Distance*, focusing exclusively on the high-curvature keypoints as surface points (Eq. 1). Despite this approach, its application to humeral implants yielded subpar results, replicating the previously encountered errors.

$$J = \frac{\sum_{k \in \mathbb{K}} (\min_{p \in Proj} (p \cdot DM_k))}{N}$$

where

\mathbb{K} = Set of all keypoints (1)

N = Number of keypoints

DM_k = Distance map for keypoint k

p = Single point on projection silhouette

To enhance the previously implemented Hamming Distance [7, 9], known for its maximal inaccuracy in cases of non-overlapping geometries, we devised a *Modified Mean Surface Distance*. This modification involved calculating the element-wise multiplication of the projection estimate ($Proj_{x,y}$) with the distance map of the target ($DM_{x,y}$), forming a new cost function (Eq. 2). However, similar to the first attempt, this approach also resulted in subpar performance.

$$J = \frac{\sum_{(x,y) \in Image} Proj_{x,y} DM_{x,y}}{\sum_{(x,y) \in Image} Proj_{x,y}} \quad (2)$$

To address these challenges, our study delves into a deeper understanding of the shape fundamentals for each arthroplasty system. This is vital for devising a method that can autonomously measure rTSA kinematics from single-plane images. Invariant Shape Descriptors offer a mathematically robust approach to describe object shapes, unaffected by changes in scale, translation, or orientation [22]. A key advantage of these descriptors lies in their ability to quantify the “nearness”, “farness”, and “uniqueness” of shapes relative to each other, represented as vector differences. Such mathematical properties have been instrumental in various object categorization tasks [19, 20, 21] and even kinematics measurement [3]. Specifically, the Invariant Angular Radial Transform Descriptor (IARTD) is notably sensitive to radial differences between shapes [13], enhancing descriptive capabilities beyond Zernike and Hu moments [11, 12, 13]. This sensitivity is especially beneficial when contour details are critical.

This paper is centered on analyzing the sensitivity of projected 2D shapes, as represented

by IARTD, to changes in their 3D orientation. Central to our investigation is understanding how subtle variations in orientation affect the projected shape, a property which is directly correlated with a shape-based optimization metric. The main goal is to highlight the differences that underscore the differences in performance of autonomous kinematics measurements between TKA and rTSA implant systems, as well as understanding any areas for improved imaging methods to boost the algorithm’s performance.

Methods

Data Collection

We obtained one manufacturer-provided 3D model for each of the following: reverse total shoulder arthroplasty (rTSA) humeral implant, rTSA glenosphere implant, total knee arthroplasty (TKA) femoral implant, and TKA tibial implant. These were used to test shape sensitivity.

Image Generation

The binary silhouette of each implant was rendered using an in-house CUDA camera model (CUDA Version 12.1) [16] to a 1024×1024 image plane. The focal length of the pinhole camera model was 1000mm and each pixel was 0.3mm. All CUDA programming was performed on an NVIDIA Quadro P2200 GPU.

Invariant Angular Radial Transform

The invariant angular radial transform descriptor (IARTD) was selected due to its sensitivity in the radial direction [13]. This sensitivity allows us to address minor changes along the contour of our projected shape, which is a desirable property for determining the minor changes in shape with respect to input orientation.

The IARTD is a complex moment calculated by summing orthogonal basis components on the unit polar disk. Each basis function has an order (n) and a repetition (p). Intuitively, the order represents concentric “rings” in our polar disk, and the repetition is the number of

95 “pie slices” in our unit disk along θ . To perform these calculations, we normalize our image
 96 such that $(0, 0)$ is at the center and $(\pm 1, \pm 1)$ are the four corners.

97 Each angular radial transform (ART) coefficient is a complex double integral (Eq. 3)
 98 over the image in polar coordinates, $f(\rho, \theta)$ multiplied by the ART basis function, $V_{np}(\rho, \theta)$
 99 (Eq. 4).

$$F_{np} = \int_0^{2\pi} \int_0^1 f(\rho, \theta) V_{np}(\rho, \theta) \rho d\rho d\theta \quad (3)$$

$$V_{np}(\rho, \theta) = A_p(\theta) R_n(\rho) \quad (4)$$

100 Our radial basis function is comprised of a complex exponential, $A_p(\theta)$ (Eq. 5), which
 101 provides rotational invariance, and a trigonometric transform, $R_p(\theta)$ (Eq. 6) to provide
 102 orthogonality.

$$A_p(\theta) = \frac{1}{2\pi} e^{jp\theta} \quad (5)$$

103

$$R_n(\rho) = \begin{cases} 1 & n = 0 \\ 2 \cos(\pi n \rho) & n \neq 0 \end{cases} \quad (6)$$

104 Lastly, in order to correct for differences in the in-plane rotation, we apply a phase-
 105 correction to each ART coefficient (Eq. 7, Eq. 8).

$$\phi'_{np} = \phi_{np} - \phi_{n,1} \quad (7)$$

$$F'_{np} = F_{np} e^{-jp\phi_{n,1}} \quad (8)$$

106 And the, the final feature vector becomes a the polar decomposition of our coefficient at
 107 each order and repetition Eq. 9. We exclude values from the first two repetitions because
 108 they contain no valuable information. To construct the full IARTD feature vector, we used
 109 values of $n = \{0, \dots, 3\}$ and $p = \{0, \dots, 8\}$.

$$IARTD = \{|F'_{np}|, \phi'_{np}\} \text{ where } n \geq 0, p \geq 2 \quad (9)$$

Shape Differences and Sensitivity

The primary goal of this section is to establish a easily interpretable value that captures the overall change from one shape to another. For clarity in representation, successive rotations were denoted as subscripts, such that $R_z R_x R_y = R_{z,x,y}$. The application of the IARTD equation to an implant at a specific input orientation $R_{z,x,y}$ was represented as $IARTD(R_{z,x,y})$. Shape differences were calculated using the central difference equation on the IARTD vector produced from two different orientations. The grid of sampled orientations had extrema of ± 30 with a step size of 5 for each of the x , y , and z axes. The “differences” along each axes were computed by applying a positive and negative rotation ($\pm \delta$) of 1 degree. And so, for every input x, y, z rotation, there will be three shape differences, one for each δ_x , δ_y or δ_z (Eq. 10). For notational brevity, we will condense the full equation down to a single $\Delta S(\delta)$, (representing $\Delta Shape$ for a differential rotation δ).

$$\Delta S(\delta)_{z,x,y} \equiv \frac{\partial IARTD(R_{z,x,y})}{\partial \delta} \propto IARTD(R_{z,x,y,+\delta}) - IARTD(R_{z,x,y,-\delta}) \quad (10)$$

Because each element of the IARTD vector is at a different scale, we must standardize each element in order to ensure accurate assessment of global behavior without analysis being dominated by a single value. We use z-score to do this, which assumes a normal distribution, but allows for some outliers if they are present.

After z-scaling, we took the Euclidean norm of each $S(\delta)_{z,x,y}$ to capture the total amount of change of that shape for a given differential rotation (Eq. 11). Our final step takes advantage of two factors: first, that our in-plane rotations are the first in our Euler sequence (z -axis), and second, that this type of rotation does not affect the in-plane shape. And so, for every x and y input rotation, we average all the values where x and y are held constant as z varies (Eq. 12). This yields our final values, which we will denote \mathbb{S} . $\mathbb{S}_{x,y}$ will have separate plots for each x , y , and z differential rotation and for each of the four implants. These plots will be compared with respect to JTML optimization performance and regions

Table 1: Average projected-shape sensitivity values for each of the implant models.

Implant Type	Average $\mathbb{S}(\delta_x)$	Average $\mathbb{S}(\delta_y)$	Average $\mathbb{S}(\delta_z)$
Humeral	8.83	4.82	7.08
Glenosphere	6.37	6.22	4.86
Femoral	6.88	8.68	4.93
Tibial	9.0	5.52	3.72

of difficulty for optimization.

$$\|S(\delta)_{z,x,y}\|_2 \quad (11)$$

$$\mathbb{S}(\delta)_{x,y} = \frac{\sum_z \|S(\delta)_{z,x,y}\|_2}{N} \quad (12)$$

Results

The humeral implant demonstrated the lowest average $\mathbb{S}(\delta_y)$ value compared to the other implant types (Fig. 1) (Table 1). This rotation represents the final rotation in our Euler rotation sequence (Z-X-Y) and captures the internal/external rotation of the humeral implant. The average δ_x value for our humeral implant was the largest among all implants (Table 1). Additionally, the surface plotted by the humeral shape sensitivity for all $\delta_{x,y,z}$ is much smoother than any of the other plots, demonstrating the relative lack of shape difference for a wide range of input orientations. Several plots showed regions with relatively low sensitivity. Specifically, the glenosphere’s δ_y sensitivity along the $y = 0$ axis (Fig. 2) and the tibial implant’s δ_y sensitivity along the $x = 0$ axis (Fig. 4). The femoral implant had the highest average sensitivity ($\frac{\mathbb{S}(\delta_x) + \mathbb{S}(\delta_y) + \mathbb{S}(\delta_z)}{3}$) among all implant types .

Discussion

The results shown align with many of our intuitive expectations about measuring the sensitivity of projected shape with respect to 3D object orientation, as well as aligned with the regions of difficulty for JTML optimization. The humeral implant demonstrated an overall

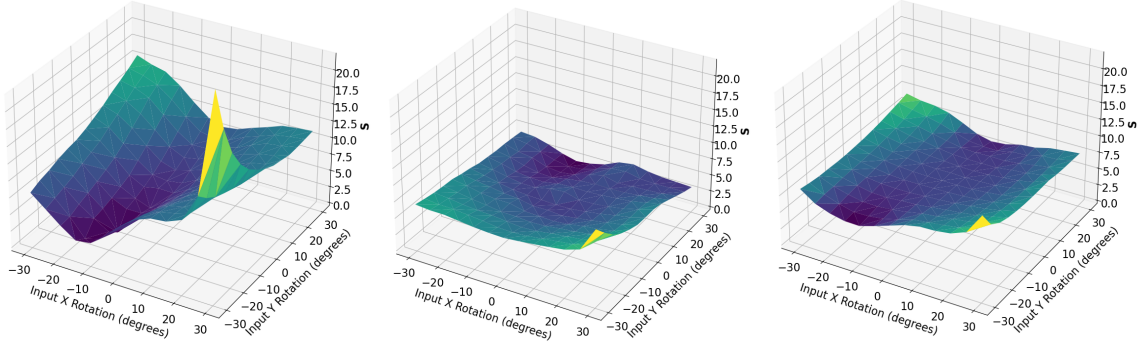


Figure 1: The \mathbb{S} plot for a humeral implant for δ rotations along the x, y, and z axis, respectively.

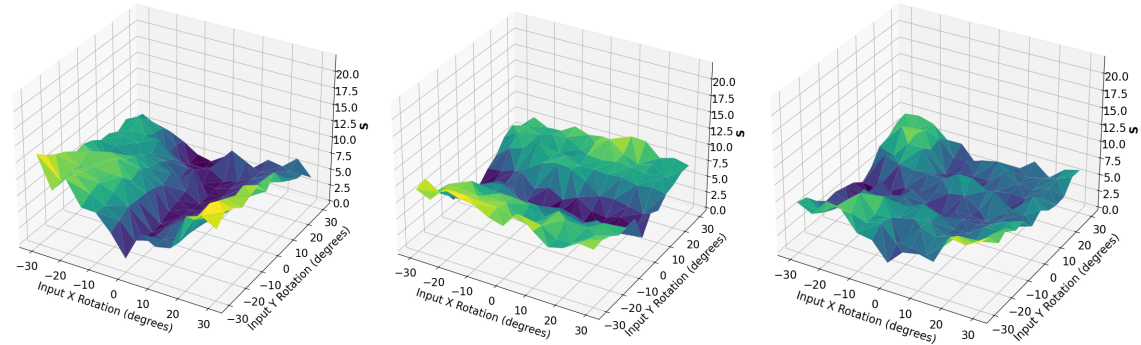


Figure 2: The \mathbb{S} plot for a glenosphere implant for δ rotations along the x, y, and z axis, respectively.

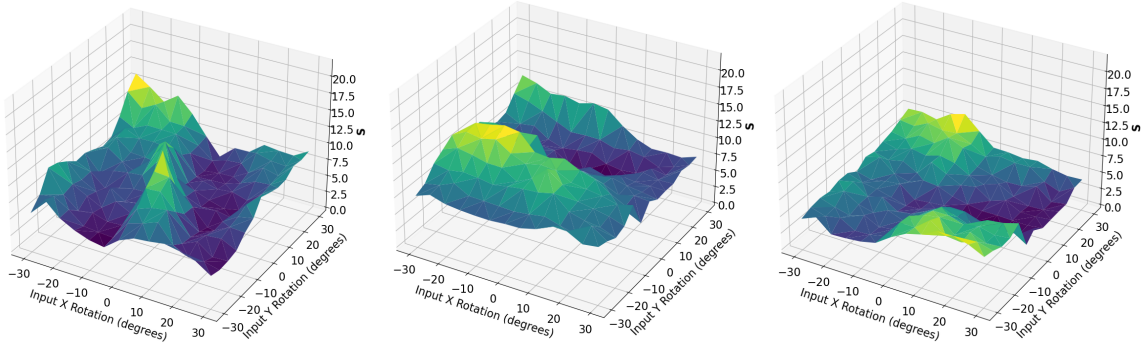


Figure 3: The \mathbb{S} plot for a femoral implant for δ rotations along the x, y, and z axis, respectively.

150 smooth and low shape sensitivity, especially for δ_y rotations (Table 1). This axis is the axis
 151 along which the humeral implant is the most cylindrical, which means that we would not
 152 expect to see a large change in the shape descriptor with minor δ_y rotations. Additionally,
 153 this is the axis which JTML had the most difficulty with.

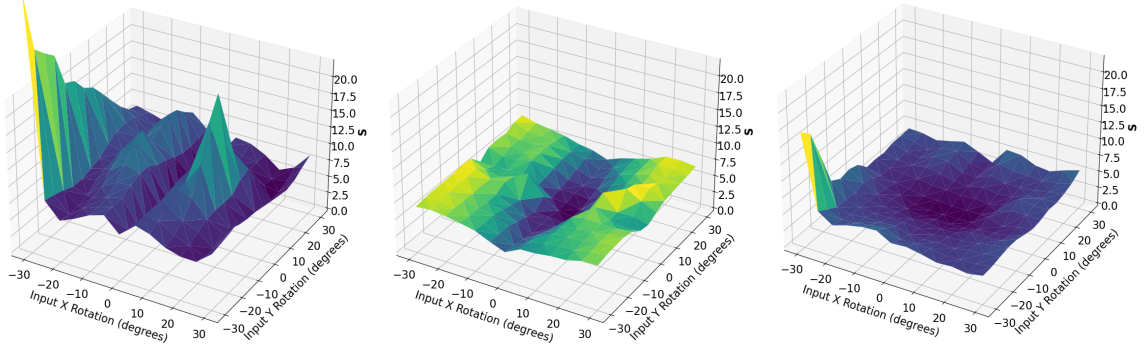


Figure 4: The \mathbb{S} plot for a tibial implant for δ rotations along the x, y, and z axis, respectively.

We see similar intuitive results in the glenosphere implant, which had the lowest average $\mathbb{S}(\delta)$ value among all implant types. This bulk of the volume of this implant is the articulation surface, which closely resembles a sphere. Because the projection of a sphere (a circle) is unchanging with respect to the orientation of a sphere, we would expect that the more closely a shape resembles a sphere, then we should expect a lower overall shape sensitivity.

We see that the shape sensitivity of the tibial implant along the δ_y rotation corroborates our intuition about symmetry traps. Along the line defined by $x = 0$, we see a consistently low shape sensitivity. This internal/external rotation axis is exactly the axis that caused issues with symmetry traps, wherein 2 distinct 3D orientations produce the same projected shape. In the context of this analysis, the ΔS would equal 0 between those two tibial orientations.

Another aspect of Joint Track Machine Learning that this study informs is the current use of Euler angles in our DIRECT-JTA optimization routine. Rather than independently varying all angles in a body-centered reference frame, which is insuitable for hyperbox creation, we are presently optimizing over a range of ordered rotations projected via the sequence $R_z R_x R_y$. As evidenced by the humeral implant’s struggles aligning the y -axis, this ordered sequence with a symmetric final axis can impede convergence.

Beyond the inherent shape sensitivities, such optimization limitations motivate exploring alternatives to Euler angles. Performing registration optimization directly on the Special Orthogonal group $SO(3)$ poses an intriguing direction. $SO(3)$ encapsulates all possible 3D rotations in a mathematically convenient structure (A *Lie Group*, which is both a manifold and a group). By optimizing on this manifold instead of using specific angle parametrizations,

issues with gimbal lock and cascade effects can be avoided. Optimization over Lie groups is an emerging subfield - establishing robust $SO(3)$ -based registration cost functions could significantly improve JTML convergence while relying less on descriptor sensitivity along certain axes.

Lastly, incorporating bone information into the optimization routine seems to be the most likely path forward for disambiguating difficult implant orientations. This study demonstrates that for specific implant geometries, there are inherent limitations to the information that can be gathered from the projected 2D shape as manifest in fluoroscopic imaging. Utilizing bone information, such as keypoints representing specific anatomic structures, would drastically increase the amount of information present during optimization, and could offer robust constraints on the possible 3D orientations of implant models.

Conclusion

This study demonstrates intrinsic differences between implant types regarding projected 2D shape sensitivity. Measurement difficulties aligned with low sensitivity along problematic axes—humeral internal rotation and tibial symmetry traps. Fundamentally, minor orientation changes yielded negligible 2D variability for near-symmetrical geometries. While inherent shape constraints limit data extractable solely from fluoroscopic silhouettes, incorporating additional image information like bone offers promise. Despite unavoidable ambiguity along select dimensions, boosting descriptor sensitivity and employing precise anatomical constraints could enable robust clinical tracking. Overall, relating optimization performance to shape response underscores routes toward accurate autonomous kinematic analysis.

References

- [1] Fred Attneave. “Some Informational Aspects of Visual Perception.” In: *Psychological Review* 61.3 (1954), pp. 183–193. ISSN: 1939-1471, 0033-295X. DOI: 10.1037/h0054663. (Visited on 11/02/2023).

- [2] Fred Attneave and Malcolm D. Arnoult. “The Quantitative Study of Shape and Pattern Perception.” In: *Psychological Bulletin* 53.6 (Nov. 1956), pp. 452–471. ISSN: 1939-1455, 0033-2909. DOI: 10.1037/h0044049. (Visited on 11/02/2023).
- [3] S.A. Banks and W.A. Hodge. “Accurate Measurement of Three-Dimensional Knee Replacement Kinematics Using Single-Plane Fluoroscopy”. In: *IEEE Transactions on Biomedical Engineering* 43.6 (June 1996), pp. 638–649. ISSN: 00189294. DOI: 10.1109/10.495283. (Visited on 03/22/2021).
- [4] Scott A. Banks and W.Andrew Hodge. “2003 Hap Paul Award Paper of the International Society for Technology in Arthroplasty”. In: *The Journal of Arthroplasty* 19.7 (Oct. 2004), pp. 809–816. ISSN: 08835403. DOI: 10.1016/j.arth.2004.04.011. (Visited on 05/13/2021).
- [5] Scott A. Banks et al. “Rationale and Results for Fixed-Bearing Pivoting Designs in Total Knee Arthroplasty”. In: *The Journal of Knee Surgery* 32.07 (July 2019), pp. 590–595. ISSN: 1538-8506, 1938-2480. DOI: 10.1055/s-0039-1679924. (Visited on 10/19/2023).
- [6] Jordan S. Broberg et al. “Validation of a Machine Learning Technique for Segmentation and Pose Estimation in Single Plane Fluoroscopy”. In: *Journal of Orthopaedic Research* (Feb. 2023). ISSN: 0736-0266, 1554-527X. DOI: 10.1002/jor.25518. (Visited on 02/13/2023).
- [7] P. D. L. Flood and Scott A. Banks. “Automated Registration of 3-D Knee Implant Models to Fluoroscopic Images Using Lipschitzian Optimization”. In: *IEEE Transactions on Medical Imaging* 37.1 (2018), pp. 326–335. DOI: 10.1109/tmi.2017.2773398.
- [8] Benjamin J. Fregly et al. “Computational Wear Prediction of a Total Knee Replacement from in Vivo Kinematics”. In: *Journal of Biomechanics* 38.2 (Feb. 2005), pp. 305–314. ISSN: 00219290. DOI: 10.1016/j.jbiomech.2004.02.013. (Visited on 08/05/2021).
- [9] Andrew J. Jensen et al. “Joint Track Machine Learning: An Autonomous Method of Measuring Total Knee Arthroplasty Kinematics From Single-Plane X-Ray Images”. In: *The Journal of Arthroplasty* 38.10 (May 2023), pp. 2068–2074. ISSN: 08835403. DOI: 10.1016/j.arth.2023.05.029. (Visited on 06/22/2023).

- [10] Andrew James Jensen et al. “Correcting Symmetric Implant Ambiguity in Measuring Total Knee Arthroplasty Kinematics from Single-Plane Fluoroscopy”. In: (In Review).
- [11] Alireza Khotanzad and Y.H. Hong. “Invariant Image Recognition by Zernike Moments”. In: *IEEE Transactions on Pattern Analysis and Machine Intelligence* 12.5 (May 1990), pp. 489–497. DOI: 10.1109/34.55109.
- [12] Whoi-Yul Kim and Yong-Sung Kim. “A Region-Based Shape Descriptor Using Zernike Moments”. In: *Signal Processing-image Communication* 16.1 (Sept. 2000), pp. 95–102. DOI: 10.1016/s0923-5965(00)00019-9.
- [13] Jong-Min Lee and Whoi-Yul Kim. “A New Shape Description Method Using Angular Radial Transform”. In: *IEICE Transactions on Information and Systems* E95.D.6 (2012), pp. 1628–1635. ISSN: 0916-8532, 1745-1361. DOI: 10.1587/transinf.E95.D.1628. (Visited on 11/21/2023).
- [14] J. C. Léger. *Menger Curvature and Rectifiability*. Apr. 1999. arXiv: math/9905212. (Visited on 01/10/2024).
- [15] M.R. Mahfouz et al. “A Robust Method for Registration of Three-Dimensional Knee Implant Models to Two-Dimensional Fluoroscopy Images”. In: *IEEE Transactions on Medical Imaging* 22.12 (Dec. 2003), pp. 1561–1574. ISSN: 0278-0062. DOI: 10.1109/TMI.2003.820027. (Visited on 03/22/2021).
- [16] John Nickolls et al. “Scalable Parallel Programming with CUDA”. In: *ACM Queue* 6.2 (Mar. 2008), pp. 40–53.
- [17] Annika Reinke et al. *Common Limitations of Image Processing Metrics: A Picture Story*. Aug. 2023. arXiv: 2104.05642 [cs, eess]. (Visited on 11/16/2023).
- [18] Annika Reinke et al. *Understanding Metric-Related Pitfalls in Image Analysis Validation*. Sept. 2023. arXiv: 2302.01790 [cs]. (Visited on 11/16/2023).
- [19] Charles W. Richard and Hooshang Hemami. “Identification of Three-Dimensional Objects Using Fourier Descriptors of the Boundary Curve”. In: *IEEE Transactions on Systems, Man, and Cybernetics* SMC-4.4 (July 1974), pp. 371–378. ISSN: 0018-9472, 2168-2909. DOI: 10.1109/TSMC.1974.5408458. (Visited on 10/25/2023).

- [20] Timothy P. Wallace and Owen R. Mitchell. “Analysis of Three-Dimensional Movement Using Fourier Descriptors”. In: *IEEE Transactions on Pattern Analysis and Machine Intelligence* PAMI-2.6 (1980), pp. 583–588. ISSN: 0162-8828. DOI: 10.1109/TPAMI.1980.6447707. (Visited on 03/04/2022).
- [21] Timothy P. Wallace and Paul A. Wintz. “An Efficient Three-Dimensional Aircraft Recognition Algorithm Using Normalized Fourier Descriptors”. In: *Computer Graphics and Image Processing* 13.2 (Jan. 1980), pp. 99–126. ISSN: 0146664X. DOI: 10.1016/S0146-664X(80)80035-9. (Visited on 03/04/2022).
- [22] Dengsheng Zhang and Guojun Lu. “Review of Shape Representation and Description Techniques”. In: *Pattern Recognition* 37.1 (Jan. 2004), pp. 1–19. DOI: 10.1016/j.patcog.2003.07.008.
- [23] S. Zuffi et al. “A Model-Based Method for the Reconstruction of Total Knee Replacement Kinematics”. In: *IEEE Transactions on Medical Imaging* 18.10 (Oct./1999), pp. 981–991. ISSN: 02780062. DOI: 10.1109/42.811310. (Visited on 09/01/2020).